JACS
JOURNAL OF THE AMERICAN CHEMICAL SOCIETY

Article

pubs.acs.org/JACS

A Stable Pentagonal Bipyramidal Dy(III) Single-Ion Magnet with a Record Magnetization Reversal Barrier over 1000 K

Jiang Liu,[†,#] Yan-Cong Chen,[†,#] Jun-Liang Liu,[*,†] Veacheslav Vieru,[‡] Liviu Ungur,[‡,§] Jian-Hua Jia,[†] Liviu F. Chibotaru,[*,‡] Yanhua Lan,[∥] Wolfgang Wernsdorfer,[*,∥] Song Gao,[⊥] Xiao-Ming Chen,[†] and Ming-Liang Tong[*,†]

[†]Key Laboratory of Bioinorganic and Synthetic Chemistry of Ministry of Education, School of Chemistry and Chemical Engineering, Sun Yat-Sen University, Guangzhou 510275, P. R. China

[‡]Theory of Nanomaterials Group and INPAC − Institute of Nanoscale Physics and Chemistry, Katholieke Universiteit Leuven, Celestijnenlaan 200F, 3001 Leuven, Belgium

[§]Theoretical Chemistry, Lund University, Getingevagen 60, 22241, Lund, Sweden

[∥]Institut Néel, CNRS & Université Grenoble Alpes, BP 166, 25 avenue des Martyrs, 38042 Grenoble Cedex 9, France

[⊥]Beijing National Laboratory for Molecular Sciences, State Key Laboratory of Rare Earth Materials Chemistry and Applications, College of Chemistry and Molecular Engineering, Peking University, Beijing 100871, P. R. China

Supporting Information

ABSTRACT: Single-molecule magnets (SMMs) with a large spin reversal barrier have been recognized to exhibit slow magnetic relaxation that can lead to a magnetic hysteresis loop. Synthesis of highly stable SMMs with both large energy barriers and significantly slow relaxation times is challenging. Here, we report two highly stable and neutral Dy(III) classical coordination compounds with pentagonal bipyramidal local geometry that exhibit SMM behavior. Weak intermolecular interactions in the undiluted single crystals are first observed for mononuclear lanthanide SMMs by micro-SQUID measurements. The investigation of magnetic relaxation reveals the thermally activated quantum tunneling of magnetization through the third excited Kramers doublet, owing to the increased axial magnetic anisotropy and weaker transverse magnetic anisotropy. As a result, pronounced magnetic hysteresis loops up to 14 K are observed, and the effective energy barrier (U_{eff} = 1025 K) for relaxation of magnetization reached a breakthrough among the SMMs.

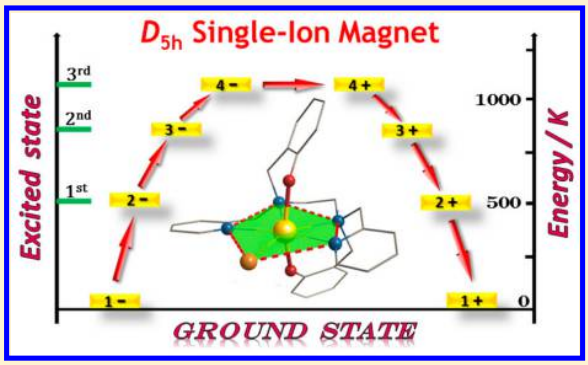

INTRODUCTION

The history of single-molecule magnets (SMMs) starts from the discovery of the nanoscale molecule, $[Mn_{12}O_{12}(OAc)_{16}(H_2O)_4]$ ($Mn_{12}Ac$)[1,2] that exhibits an extremely slow magnetic relaxation such that it can show magnetic hysteresis below the blocking temperature (T_B). This behavior can potentially be utilized for the nontrivial applications in ultrahigh-density information storage and molecular spintronics.[3,4] For further development of this field, it is important to obtain large energy barriers that help to retain either one of the two magnetic states for extending the relaxation time as well as to be stable enough for preventing decomposition, suffering chemical modification and depositing on the surface at spintronics domain. The solvent-free and stable compounds can also ensure that the measured properties are exactly from the molecules obtained by X-ray diffraction, minimizing the chances of appearing complicated behaviors from the significant decomposition and/or distortion of the structure.

Owing to the large single-ion magnetic anisotropy arising from the strong intrinsic spin−orbit coupling as well as the crystal-field effect, f-block compounds including those with a single paramagnetic center (single-ion magnets, SIMs) are quite promising for achieving the goal of high-performance SMMs and thus have become popular recently.[5−16] However, in contrast to the d-block polynuclear SMMs such as $Mn_{12}Ac$, a substantial majority of the f-block SMMs favor the resonant spin−lattice relaxation via the first excited $\pm m_J$ state (only two f-block SMMs exhibit relaxation through the second $\pm m_J$ excited[12,15] and one through the third and fourth $\pm m_J$ excited states[16]), which lowers the effective energy barrier for magnetization reversal. Thus, it appears that one of the current challenges is to search for an approach toward the large-energy-barrier f-block SMMs that relax through the higher $\pm m_J$ states.

Received: March 11, 2016
Published: April 7, 2016

DOI: 10.1021/jacs.6b02638
J. Am. Chem. Soc. 2016, 138, 5441−5450

Additionally, according to the general understanding, the limit of very strong magnetic axiality is achieved for low-coordinated lanthanide complexes, containing in its closest neighborhood one single ligand atom (Ln−L) or two ligand atoms lying on a common L−Ln−L axis. Such low coordination numbers are not typical at all for lanthanides, which is the main difficulty toward very large relaxation barriers, amounting to several thousand wavenumbers, as predicted by the theory.[17] Most of the low-coordinated lanthanide-containing SMMs with large effective energy barriers and blocking temperatures are organometallic or air-sensitive compounds. For example, the 2p-4f $\{Tb_2(N_2^{3-})\}$ SMM exhibits high blocking temperature (T_B = 14 K) and a huge magnetic hysteresis.[10,11] However, these compounds are generally not easy to synthesize and are also unstable in heat and air. Furthermore, for the well-known homoleptic ($[Tb(III)(Pc)_2]$) and heteroleptic ($[Tb(III)(Pc)(Pc')]$) Tb(III) bis-(phthalocyaninate) SMMs, despite the high stability and large energy barriers (up to 938 K for one of the derivatives), the blocking temperature is still quite low (<2 K) because of the fast quantum tunneling of magnetization (QTM).[14]

The coordination environment of the single lanthanide ion is of crucial importance and should be a strong focus of SMM research, for example, Dy(III) ion with short and negative-charged axially coordinating atoms in D_{5h} local symmetry was shown to be advantageous for suppression of QTM and enhancement of the effective energy barrier, owing to maximize the level splitting, the elimination of the off-diagonal matrix elements of the crystal-field Hamiltonians, and the stabilization of the largest $\pm m_J$ state ($m_J = \pm 15/2$).[13] Accordingly, we believe that pentagonal bipyramidal Dy(III) coordination compounds are promising candidates for designing high-performance SMMs.

Here, we report an investigation of two Dy(III) SIMs, [Dy(bbpen)X] (X = Cl, **1**; Br, **2**; H_2bbpen = *N*,*N*′-bis(2-hydroxybenzyl)-*N*,*N*′-bis(2-methylpyridyl)ethylenediamine), with approximate D_{5h} local symmetry. These are air and heat stable, which is quite beneficial for device applications as building blocks in spintronics[3,4] and SMM engineering. Magnetic studies and ab initio calculations reveal that the relaxation pathway of the magnetization proceeds through the second excited Kramers doublet (KD) for **1** and the third excited state for the more linear **2**, owing to the introduction of a stronger axial crystal field and a weaker transverse crystal field, and leading to a revolutionary energy barrier (>1000 K), accompanied by a hysteresis of up to 14 K. This work proposes a practical way to achieve large energy barrier, while keeping the usual high coordination numbers. The idea is to design such an environment that will have two closely spaced axial atoms and five distant ones in the equatorial plane. Since the effect of the latter is not negligible, they should produce an equatorial field as symmetric as possible. The two complexes studied here follow fully this idea. Moreover, a more symmetric compound **2**, whose ligand field is closer to D_{5h} symmetry of an ideal pentagonal bipyramid, shows a stronger axiality and a higher anisotropy barrier.

RESULTS AND DISCUSSION

Compounds **1** and **2** are readily isolated under aerobic conditions through different reaction routes: slow evaporation and solvothermal synthesis, respectively. The resulting neutral molecules are extremely stable even when heated up to 600 K (**1**) and 615 K (**2**) (Figure S1). In addition, no crystallographic solvent molecules are present for both compounds; this greatly reduces the destabilization and is conducive for performing the measurements.

Crystal Structures. Single-crystal X-ray diffraction confirmed that the two compounds are isostructural (Table S1). Compounds **1** and **2** crystallize in the orthorhombic space group $C222_1$ with a similar asymmetric unit containing only one-half of Dy(III) ion, one-half of Cl^- or Br^- (respectively for **1** or **2**), and one-half of $bbpen^{2-}$ ligand, as depicted in Figure 1

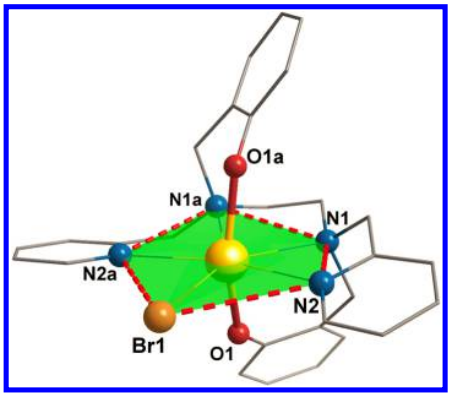

Figure 1. Molecular structure for **2**. The equatorial plane of pentagonal bipyramidal coordination sphere is highlighted. Dy, yellow; Br, brown; O, red; N, blue; C, gray. Hydrogen atoms are omitted for clarity. Symmetry transformations used to generate equivalent atoms: (a) $-x + 1, y, -z + 1/2$.

(and Figure S2). There are four molecules in the unit cell, two of which are in the unit cell and four half of which are on the two faces of the cell. The symmetry operations connecting these molecules are either translation and rotation by 180° around *c* axis. The shortest distance between the neighboring molecules is respectively 8.5001(6) Å for **1** and 8.5482(6) Å for **2**, with the weak intermolecular interactions via C−H···π, Cl/Br···H−C, and O···H−C contacts (Table S2 and Figure S5).

The Dy(III) site in **2** possesses a distorted pentagonal bipyramidal coordination sphere (Table S3) occupied by one Br^-, two O, and four N atoms from a single $bbpen^{2-}$ ligand. Two phenol O atoms are negatively charged and axially coordinated to Dy(III) with the very short axial Dy1−O1 distance of 2.166(4) Å for **1** and 2.163(3) Å for **2** and O(1)−Dy(1)−O(1a) bond angle of 154.3(2)° for **1** and 155.8(2)° for **2**, indicating that Dy−O bond length of the two compounds is similar while the O−Dy−O bond angle is more linear for **2**. One Br(Cl) and four N atoms in the equatorial plane (Figure 1) are all weakly coordinated with the Dy(III) as indicated by the long average Dy−N distances of 2.586 Å for **2** (2.583 Å for **1**) and an even longer Dy1−Br1 (Dy1−Cl1) bond length of 2.8515(6) Å in **2** (2.6818(16) Å in **1**). It is important to note that no crystallographic solvent molecules are present.

Magnetic Characterization. Temperature-dependent magnetic direct current (dc) susceptibility measurements were performed on polycrystalline samples of **1** and **2** under 1 kOe applied field (Figure 2). The room temperature $\chi_m T$ values are 13.74 and 13.36 cm^3 K mol^{-1} for **1** and **2**, respectively, somewhat smaller than the expected values (S = 5/2, L = 5, $^6H_{15/2}$, J = 15/2, g = 4/3, 14.17 cm^3 mol^{-1} K). On cooling, both $\chi_m T$ products decrease slightly, suggesting the presence of strong crystal-field splitting with far-separated excited Kramers doublets. Field-cooled (FC) and zero-field-

DOI: 10.1021/jacs.6b02638
J. Am. Chem. Soc. 2016, 138, 5441−5450

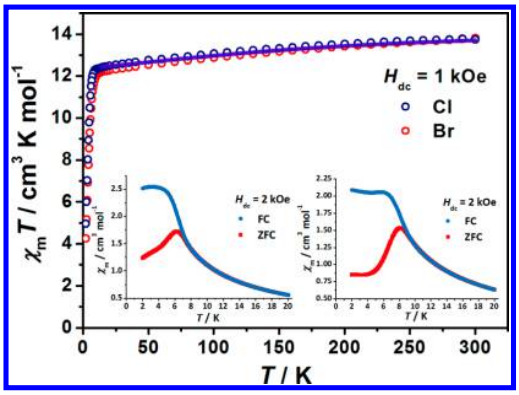

Figure 2. Variable-temperature molar magnetic susceptibility data for **1** and **2**. Solid lines correspond to the ab initio calculation results. Inset: plot of magnetic susceptibility vs temperature during FC (blue) and ZFC (red) measurements for **1** (left) and **2** (right).

cooled (ZFC) magnetic susceptibility (inset of Figure 2) shows divergences at 7.5 and 9.5 K for **1** and **2**, respectively, which are indicative of magnetization blocking.

Dynamics magnetic measurements were carried out in zero dc field to probe the slow magnetic relaxation behavior for compounds **1** and **2**. The temperature and frequency dependences of the in-phase (χ_m') and out-of-phase (χ_m'') alternating current (ac) susceptibility components show typical SMM behavior (Figures 3a,b, 4a,b and S7). The maximum for χ_m'' (1488 Hz) appears at 50 and 60 K for **1** and **2**, respectively. The relaxation times (τ) can thus be extracted using the generalized Debye model (Figures 3c,d, 4c,d, and S8, and S9),[18a] giving narrow relaxation time distributions ($\alpha \leq 0.06$). The relaxation times for **1** and **2** at high temperatures obey an Arrhenius law with an effective energy barrier for relaxation U_{eff}/k_B = 708 K (492 cm^{-1}) and $\tau_0 = 9.46 \times 10^{-11}$ s for **1** and U_{eff}/k_B = 1025 K (712 cm^{-1}) and $\tau_0 = 4.21 \times 10^{-12}$ s for **2** (Figures 3 and 4). Remarkably, the effective energy barrier and the ac-peak temperature for **2** are both the largest known values for all SMMs (Table S4). According to the well-known oblate-prolate model,[18b] the free ion electron density of the Dy(III) ion with $m_J = \pm 15/2$ ground KD has an oblate shape, favoring a strong axial crystal field and a weak transverse crystal field. Compounds **1** and **2** both meet this criterion by introducing a short axial Dy−O bond and weakly coordinated atoms in the transverse plane. A more axial crystal field and a weaker transverse Dy−Br bond (see the details in the section of ab initio calculations) lead to a higher U_{eff} value for **2** than that for **1**.

Faster relaxation processes and QTM that do not obey the Arrhenius law appear in the low-temperature region, such as Raman or direct relaxation, limiting concurrently the relaxation time of compound **1** on a millisecond time scale (Figures 3d). As expected, compound **2** shows much stronger magnetization blocking, with relaxation times (41 s at 4 K) several orders of magnitude longer than those in **1** even at zero applied dc field, which is rarely slow in SMMs domain.[10] In the presence of a 2 kOe dc field, a large increase (Figures S10 and S11) of the relaxation time is observed for both compounds, with values of 320(1) s for **1** and 1825(1) s for **2** at 4 K (Figures 3d and Figure 4d).

Magnetic hysteresis (Figure 5) loops are clearly open at zero field up to 8 K for **1** and even up to 14 K for **2**, suggesting that

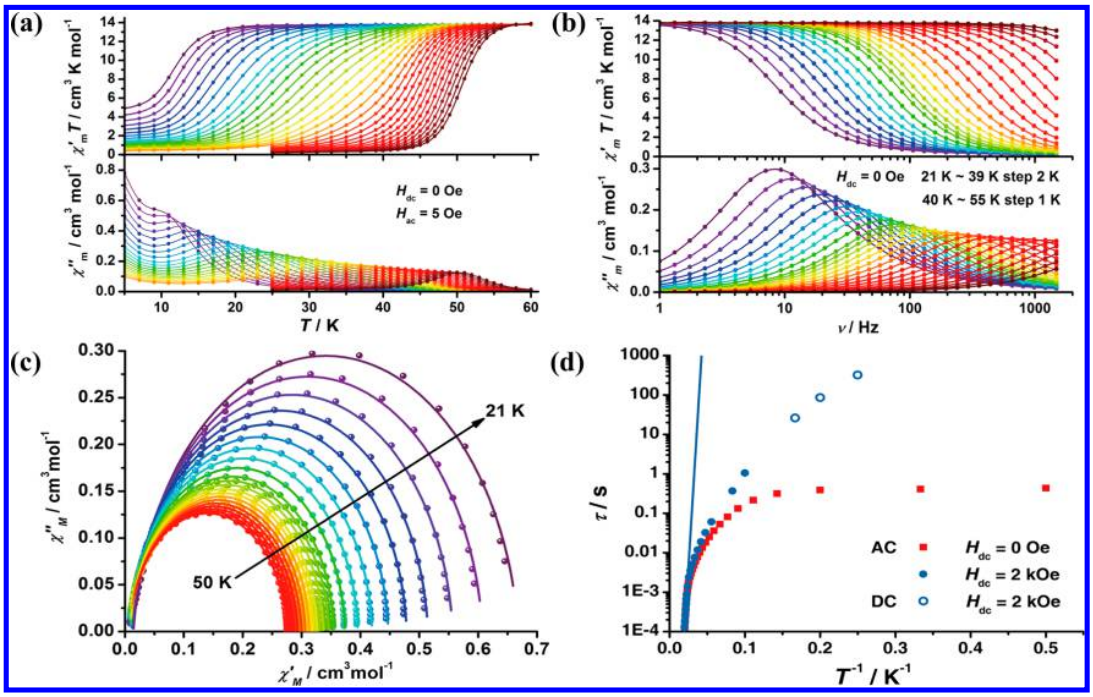

Figure 3. Alternating current molar magnetic susceptibilities, Cole−Cole plot, and magnetic relaxation for **1**. (a, b) Temperature and frequency dependence of the in-phase ($\chi_m'T$) product and out-of-phase (χ_m'') in zero dc field for **1** with the ac frequency of 1−1488 Hz. (c) The α value range is from 0.02 to 0.06 between 21 and 50 K. (d) Temperature dependence of the magnetic relaxation time τ under 0 Oe and 2 kOe is shown as τ versus T^{-1}, where the values under 2 kOe below 10 K were obtained from relaxation measurements of the dc magnetization (open circles). The solid lines correspond to a fit to the Arrhenius expression affording U_{eff}/k_B = 708 K (492 cm^{-1}) and $\tau_0 = 9.46 \times 10^{-11}$ s. The Arrhenius plot enlarged at high-temperature regime is shown in Figure S15a.

DOI: 10.1021/jacs.6b02638
J. Am. Chem. Soc. 2016, 138, 5441−5450

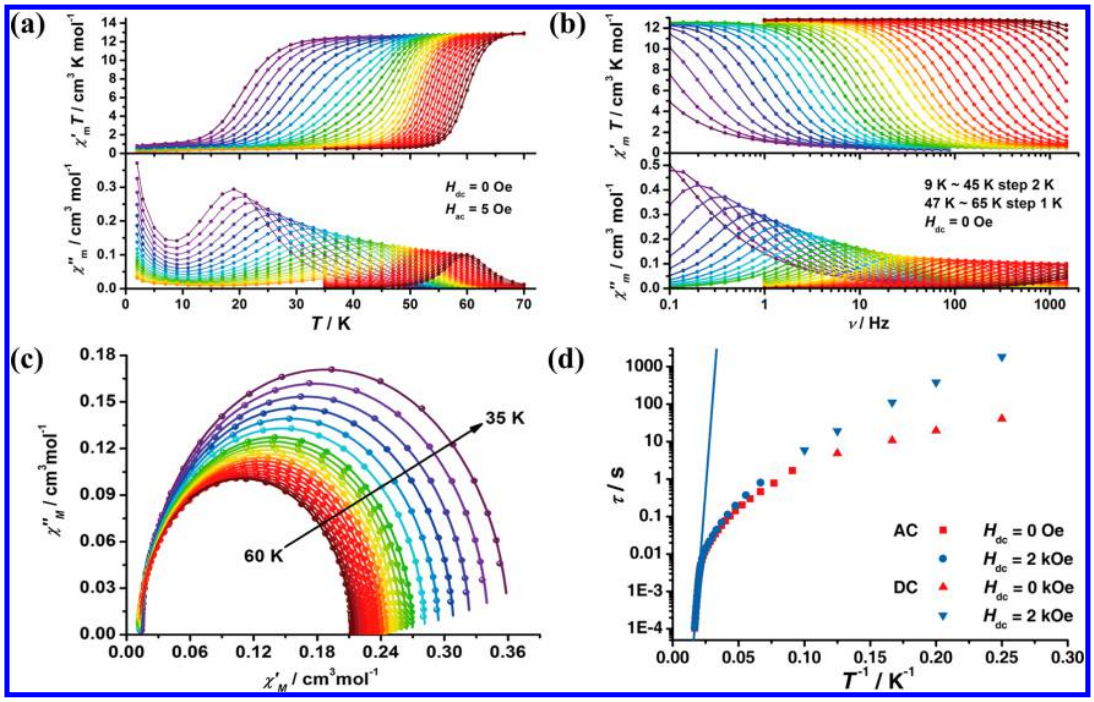

Figure 4. Alternating current molar magnetic susceptibilities, Cole−Cole plot, and magnetic relaxation for **2**. (a, b) Temperature and frequency dependence of the in-phase ($\chi_m'T$) product and out-of-phase (χ_m'') in zero dc field for **2** with the ac frequency of 1−1488 Hz. (c) The α value range is from 0.00 to 0.02 between 35 and 60 K. (d) Temperature dependence of the magnetic relaxation time τ under 0 Oe and 2 kOe is shown as τ versus T^{-1}, where the values below 10 K were obtained from relaxation measurements of the dc magnetization (filled triangles). The solid lines correspond to a fit to the Arrhenius expression affording U_{eff}/k_B = 1025 K (712 cm^{-1}) and $\tau_0 = 4.21 \times 10^{-12}$ s. The Arrhenius plot enlarged at high-temperature regime is shown in Figure S15b.

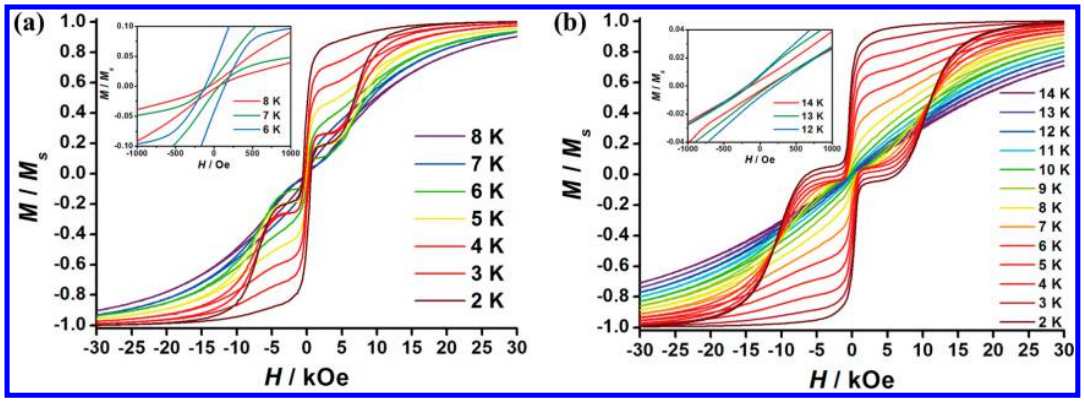

Figure 5. Variable-field magnetization data for **1** and **2**. Magnetic hysteresis loops were measured at a sweep rate of 0.02 T s^{-1} in the 2−8 K temperature range for the powder sample **1** (a) and from 2 to 14 K for the powder sample **2** (b).

they are among the highest hysteresis temperature SMMs,[10,19,20] owing to the very slow relaxation times for both compounds (Table S4). It is worth noting that the hysteresis loops were observed at temperatures higher than the divergence of the FC/ZFC (7.5 K for **1** and 9.5 K for **2**), which is due to the difference of the scan speed of the hysteresis loops and the relaxation times.

In order to understand the influence of the intermolecular interactions in **1** and **2**, we have performed low-temperature hysteresis loop measurements on single crystals using a micro-SQUID array.[21] As described in the structural part, two crystallographically distinct molecules exist in each unit cell providing two different orientations of the magnetic axes. When the external magnetic field is applied along the average projection of these two orientations (Figure 6 inset), depending on the direction of the applied field, either an antiferromagnetic or ferromagnetic interaction is observed in the hysteresis loop measurements, see Figure 6 the Cl compound **1**. Concerning the Br compound **2**, we measured hysteresis loops only along the ferromagnetic projection (Figure 7) because of the field limitation of the micro-SQUID setup (1.4 T).

In general, the width of hysteresis loops for both compounds is strongly temperature and sweep rate dependent (Figures 6, 7, and S17−S19), which is the typical behavior for SIMs. The width of the hysteresis loops for the Br case (Figures 7a) is much more pronounced than that for the Cl compound (Figures 6a), consistent with its higher energy barrier determined from the ac susceptibilities measurements and its

DOI: 10.1021/jacs.6b02638
J. Am. Chem. Soc. 2016, 138, 5441−5450

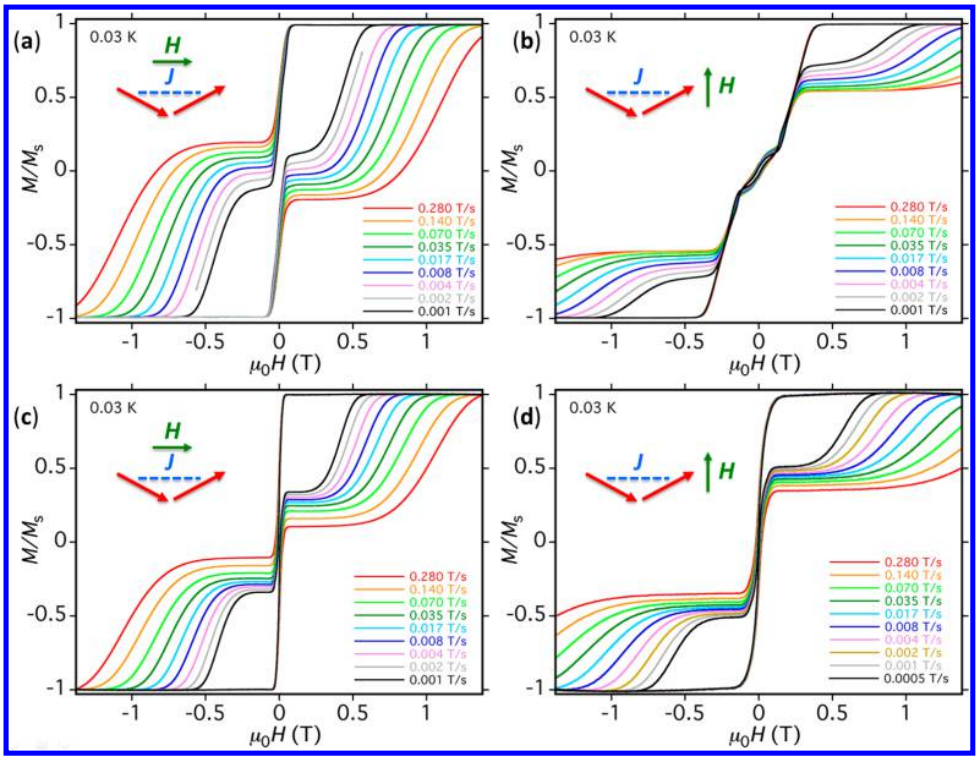

Figure 6. Magnetization vs magnetic-field hysteresis loops for **1** (a, b) and Dy@**3** (c, d) single crystals at the indicated field sweep rates and a fixed temperature of 0.03 K. Insets: The two red arrows represent the orientations of the magnetic axes of the Dy(III) ions, which are coupled by the exchange interaction *J*; the green arrow indicates the direction of the applied magnetic field, where in (a) and (c) the magnetic field is applied along the ferromagnetic projection and in (b) and (d) the field is applied along the antiferromagnetic projection. The magnetization is normalized to its saturation value M_S at 1.4 T.

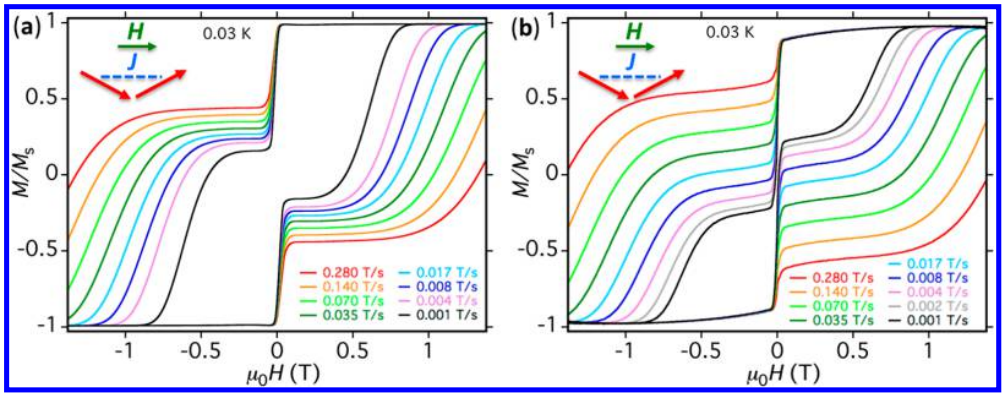

Figure 7. Magnetization vs magnetic-field hysteresis loops for **2** (a) and Dy@**4** (b) single crystals at the indicated field sweep rates and a fixed temperature of 0.03 K. The magnetic field is applied along the ferromagnetic projection, as indicated in the insets (see also figure caption of Figure 6). The magnetization is normalized to its saturation value M_S at 1.4 T.

slower relaxation. The zero-field step increases very rapidly in both cases when the field is applied along the ferromagnetic projection (Figures 6a and 7a). On the other hand when the field is applied transverse to the ferromagnetic projection, i.e., along the antiferromagnetic projection (Figure 6b), the loops exhibit a double S-shape establishing the presence of antiferromagnetic interactions between the two Dy(III) ions with different orientations. It is likely that these interactions are mediated by the C−H···π, Cl/Br···H−C, and O···H−C contacts. The strength of these intermolecular exchange interactions can be quantified from the inflection point of the first step, which is located at ±0.3 T. Based on the equation $zJ = g_J\mu_B\mu_0 H \sin(\Phi/2)/[2m_J \cos(\Phi)]$, where $m_J = 15/2$, $g_J = 4/3$, and $\Phi = 47.6°$ is the angle between the two easy axes directions obtained from the ab initio calculations (see Figures 9 and S5), the interaction is determined to be about 0.011 K. Such a weak supramolecular interaction has also been observed in many so-called exchanged-biased SMMs.[22−24]

In order to reduce the influence of intermolecular interactions on the spin relaxation dynamics and unequivocally confirm SIM behavior, we prepared isostructural and diamagnetic yttrium analogues [Y(bbpen)Cl] (**3**) and [Y(bbpen)Br] (**4**) and experimentally investigated the effect of chemical dilution. Magnetic measurements were performed on

DOI: 10.1021/jacs.6b02638
J. Am. Chem. Soc. 2016, 138, 5441−5450

the diluted samples, Dy@**3** and Dy@**4**, in which the individual Dy(5.7 ± 0.5%) ions are magnetically isolated by the yttrium analogues (Figures S12−14 and S20−21). It is worth noting that the hysteresis for Dy@**3** is now observed up to 10 K at a scan rate of 0.02 T s^{-1} under zero field (Figure S14a). The absence of obvious upturned tails at lower temperature in the plots of χ_m'' vs T (Figures S12a and S13a) shows that this interaction-driven thermally assisted ground-state tunneling is reduced in the diluted samples. This kind of observation is similar to previous studies on SIMs.[7,9,25] Although the Arrhenius fitting of the relaxation time gives similar values of U_{eff} and τ_0 (Figure S15), the relaxation times obtained from ac and dc measurements at low temperature (4 K) are slower than those of the undiluted samples (Figures S12d and S13d) due to the suppression of interaction driven QTM effects. This dilution experiment further confirms that the SIM behavior observed in **1** and **2** is of molecular origin and is related to the single ion magnetic behavior of Dy(III) itself.

For the relaxation time products under zero dc field, the direct process can be neglected, making the total relaxation rates mainly remain the Orbach process and Raman process: $\tau_{total}^{-1} = \tau_0^{-1}\exp(-U_{eff}/k_BT) + CT^n$.[26−28] In order to further verify the domination of the Orbach process at high temperature, relaxation time vs temperature is plotted in log−log scale (Figure S16), whose slope indicates the Raman exponent is respectively n = 15 for **1** and Dy@**3** and n = 18 for **2** and Dy@**4**. The anomalously large Raman exponents ($n \gg 9$)[26−28] exclude the possibility of the presence of the Raman process in the high-temperature range, suggesting the Orbach one is dominant. In the low-temperature range, the Raman process still plays an important role in the relaxation times. Figure 8 is shown as the best-fit curves include both processes,

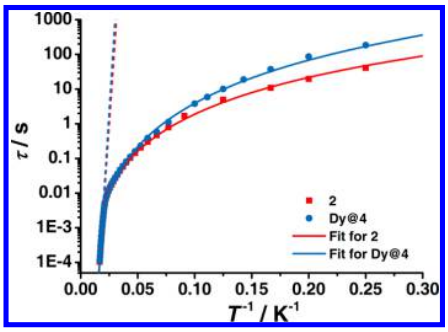

Figure 8. Magnetic relaxation for **2** and Dy@**4**. Temperature dependence of the magnetic relaxation time τ under 0 Oe is shown as τ versus T^{-1}. The dash lines and the solid lines are respectively corresponding to the part of Orbach process and the best fits that include both Orbach process and Raman process.

given U_{eff}/k_B = 1088 K (756 cm^{-1}), $\tau_0 = 1.51 \times 10^{-12}$ s, $C = 1.49 \times 10^{-4}$ s^{-1} $K^{-3.5}$, and n = 3.5 for **2** and U_{eff}/k_B = 1191 K (828 cm^{-1}), $\tau_0 = 2.71 \times 10^{-13}$ s, $C = 1.75 \times 10^{-5}$ s^{-1} $K^{-4.2}$, and n = 4.2 for Dy@**4**. However, for **1** and Dy@**3**, the relaxation times at low temperatures cannot be fitted well, possibly due to the existence of strong QTM.

In addition to the relaxation time and the relaxation process discussed above, magnetic site dilution also has an impact on the shape of the hysteresis loops. In contrast to the undiluted systems, the most striking feature is found that at low temperatures (0.03 K), the fast magnetization relaxation due to the ground-state QTM becomes obvious at zero magnetic field for the diluted systems. As shown in Figures 6c,d and 7b, the quantum tunneling becomes so fast that almost no loop opening is observed at these low temperatures. Additionally, the loops of the diluted systems around zero field become much sharper now because the dipolar and intermolecular interactions are vanishing and the broadening effect is weak. In other words, as the temperature is lowered, the diluted systems display widening of the steps of butterfly shaped loops, which have the same effect as other SMMs reported.[12] This effect can be clearly evidenced in the Dy@**3** case. We mounted the diluted crystals in the same orientation and applied the magnetic field in the same projection as those done for the undiluted ones (Figure 6). Upon dilution, the loops collected in either the antiferromagnetic or ferromagnetic projection exhibit almost the same shape by widening up the butterfly shaped loops.

Ab Initio Calculations. To further investigate the differences in magnetic properties of **1** and **2**, CASSCF/SO-RASSI/SINGLE_ANISO ab initio calculations were performed using the MOLCAS 8.0 program.[29−31] The experimentally determined structures of the analyzed compounds were used in all calculations. Detailed information about the computational details is given in the Supporting Information, whereas here we only present the results obtained using the largest basis set. The computed energy of the low-lying KDs of the Dy centers as well as their g-tensors are shown in Table 1. Ab initio

Table 1. Energy (cm^{-1}) of the Lowest KDs and Their g-Tensors

1			2		
g		energy	g		energy
g_x	0.0011		g_x	0.0005	
g_y	0.0014	0	g_y	0.0006	0
g_z	19.8747		g_z	19.8808	
g_x	0.1120		g_x	0.0625	
g_y	0.1643	382	g_y	0.0795	394
g_z	16.9117		g_z	16.9847	
g_x	2.2581		g_x	0.8681	
g_y	5.3621	586	g_y	1.5588	627
g_z	11.4210		g_z	13.5098	
g_x	7.3811		g_x	4.7427	
g_y	6.9119	655	g_y	6.0378	721
g_z	2.0243		g_z	9.8203	

predictions for these compounds are accurate as can be inferred from an almost perfect agreement of the calculated magnetic properties with the experimentally obtained values (Figures 2 and S6).

Examination of the data in Table 1 shows that calculated KDs are more axial in **2** than in **1**, explaining the more pronounced SMM behavior for the former compound. The orientation of the main magnetic axis of the ground KD in **2** is shown in Figure 9 and is very similar to the orientation of the main anisotropy axis in **1**. In both compounds, the main magnetic axis passes close to the oxygen atoms (Figure 9). To understand why the ground KD in **2** is more axial than in **1**, we analyze the crystal-field parameters of both compounds (Table 2). We find that the $B(2,0)$ parameter is larger in **2** than in **1**, explaining a stronger crystal-field splitting in this compound (Table 1). At the same time, the nonaxial parameters, notably the $B(2,q)$, are larger in **1**, explaining the more axial KDs in **2**. The differences in crystal-field parameters are caused by

DOI: 10.1021/jacs.6b02638
J. Am. Chem. Soc. 2016, 138, 5441−5450

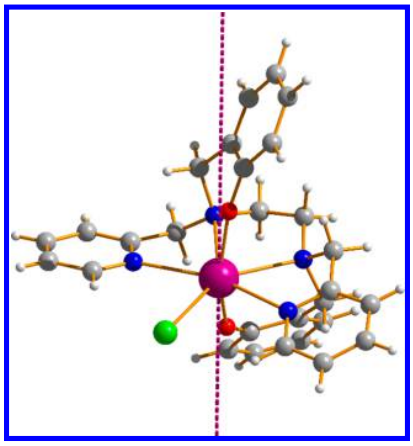

Figure 9. Molecular structure for **2**. Color code: Dy, purple; Br, lime; O, red; N, blue; C, gray; H, white. Dashed line shows the orientation of the main magnetic axis in the ground Kramers doublet.

Table 2. Ab Initio Computed Crystal-Field Parameters[a]

		$B(k,q)$	
k	q	**1**	**2**
2	−2	0.58×10^{-02}	0.44×10^{-02}
2	−1	-0.27×10^{-02}	-0.44×10^{-02}
2	0	-0.40×10^{01}	-0.44×10^{01}
2	1	0.75	0.65
2	2	0.15×10^{01}	0.10×10^{01}
4	−4	-0.76×10^{-04}	-0.63×10^{-04}
4	−3	0.19×10^{-03}	0.23×10^{-03}
4	−2	-0.64×10^{-04}	-0.61×10^{-04}
4	−1	-0.55×10^{-04}	-0.71×10^{-04}
4	0	-0.10×10^{-01}	-0.10×10^{-01}
4	1	-0.66×10^{-02}	-0.61×10^{-02}
4	2	0.52×10^{-02}	0.51×10^{-02}
4	3	0.21×10^{-01}	0.20×10^{-01}
4	4	-0.62×10^{-02}	-0.38×10^{-02}
6	−6	0.42×10^{-05}	0.54×10^{-05}
6	−5	-0.84×10^{-06}	-0.82×10^{-06}
6	−4	-0.67×10^{-06}	-0.54×10^{-06}
6	−3	0.14×10^{-05}	0.16×10^{-05}
6	−2	-0.17×10^{-05}	-0.19×10^{-05}
6	−1	0.35×10^{-07}	0.89×10^{-07}
6	0	-0.20×10^{-06}	0.34×10^{-05}
6	1	0.41×10^{-04}	0.41×10^{-04}
6	2	-0.95×10^{-04}	-0.86×10^{-04}
6	3	0.15×10^{-03}	0.13×10^{-03}
6	4	-0.11×10^{-05}	0.59×10^{-05}
6	5	-0.61×10^{-04}	-0.50×10^{-04}
6	6	0.25×10^{-03}	0.25×10^{-03}

[a]Only the ranks k = 2, 4, and 6 are shown, higher ranks are much smaller and not shown here. Note that the limitation to the sixth rank of Stevens operators arises only in phenomenological crystal field theory, approximating the ligand-field states by pure atomic 4f orbitals, i.e., neglecting completely their hybridization to the ligand orbitals. The ab initio approach employed here is free from this restriction, therefore it gives ranks higher than six for the crystal field of lanthanide complexes.

structural differences between the two compounds. For example, the Dy−O distance is slightly shorter (Table S2), and the O−Dy−O angle is closer to 180° in **2**. Furthermore, Cl is closer to Dy than Br, and it therefore makes a greater contribution to the transverse crystal-field parameters $B(k,q)$.

A recently proposed methodology has been applied to determine the structure of the magnetization blocking barrier in the investigated compounds.[32] Inspection of Figure 10 shows

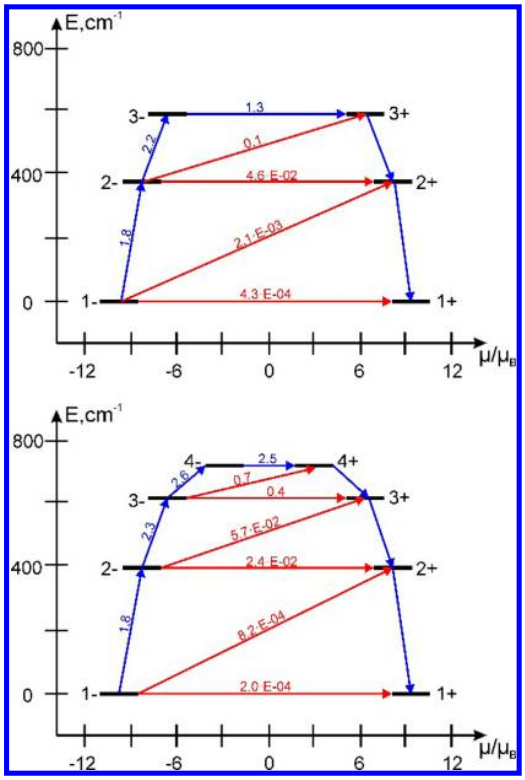

Figure 10. Magnetization blocking barrier in **1** (up) and **2** (down). Exchange states are arranged according to the values of their magnetic moments (bold horizontal black lines). Arrows show the transition between the states, while the numbers above the arrows are the corresponding average matrix element of the magnetic moment ($\bar{\mu}$).[31] Relaxation pathway is outlined by arrows containing the largest $\bar{\mu}$ (blue arrows).

that average magnetic moment matrix elements connecting opposite components of the KDs ($\bar{\mu}$) are smaller in **2** than in **1**, as expected from the more axial g-tensor of the former compound. Interestingly, in **1**, the relaxation path (blue arrows in Figure 10) of the blocking barrier proceeds through a second excited KD at 586 cm^{-1}, while in **2**, the relaxation path proceeds through the third excited KD at 721 cm^{-1}. At a first glance, the matrix element connecting the opposite components of the second excited KD in **2** is sufficiently large (0.4 μ_B) to suggest that this doublet is the top of the barrier. However, this matrix element is much larger (2.5 μ_B) for the next doublet, so that tunneling through barrier can take place at this doublet for a sufficiently high temperature. Indeed, the rate of thermally assisted tunneling transition (TAT) is the product of the Boltzmann population of a given doublet and the rate of incoherent tunneling transition between the components with opposite magnetization.[33] Because the latter is roughly proportional to the square of $\bar{\mu}$ of the corresponding doublet state,[32] the rate of TAT is proportional to $e^{-E/kT}\bar{\mu}^2$, where E is the energy of the doublet and k is the Boltzmann constant. Using the data from Table 1 and Figure 10, for the ratio of

DOI: 10.1021/jacs.6b02638
J. Am. Chem. Soc. 2016, 138, 5441−5450

TAT rates in the third and second excited KD of **2** at 60 K (the temperature preceding the linear domain for the $\ln(\tau)$ vs $1/T$ curve in Figure 4d), we obtain $P_{4-\rightarrow 4+}/P_{3-\rightarrow 3+} \approx 4$. This ratio will increase with a further increase of T, implying that the activated relaxation via the third KD becomes dominant in the temperature domain where a linear $\ln(\tau)$ vs $1/T$ dependence is observed. Therefore, the slope of this linear dependence (the height of the barrier) corresponds to the energy of the third doublet in full agreement with ab initio calculations (712 vs 721 cm^{-1}). On the other hand, in **1** the matrix element $\bar{\mu}$ connecting the 3− and 3+ states is sufficiently large (1.3 μ_B) to guarantee dominant TAT relaxation via this doublet in the high-T domain up to the highest investigated temperatures. The discrepancy between the calculated energy of the second KD (586 cm^{-1}) and the experimentally extracted height of the barrier (492 cm^{-1}) may be related to the fact that the linear domain in the $\ln(\tau)$ vs $1/T$ dependence has not yet been reached; this is indicated by the presence of curvature in Figure 3 up to highest investigated temperatures. The above analysis reveals the mechanism by which these two very similar compounds exhibit qualitatively different relaxation behaviors caused solely by the subtle differences between their structures.

Since the discovery of the first SMM,[1,2] it was clear that besides the height of the barriers also their opacity (impenetrability) is of crucial importance for achieving long relaxation times in a wide temperature range. The latter requires the presence of several intermediate excited states for which QTM is blocked. The complexes presented here are generic structures suitable for achieving this goal because they entail a strong axial and weak equatorial ligand field. A further progress toward enhancing the axial and weakening the equatorial ligand field will approach the complexes of this type to the ideal limit where virtually all excited states originating from the ground J-multiplet of the Ln ion will constitute the blocking barrier, the latter reaching the height of several thousand wavenumbers.[17]

CONCLUSION

In the present work, highly stable pentagonal bipyramid Dy(III) molecules were obtained by a facile synthesis. Magnetization reversal barriers corresponding to relaxation via the second and the third excited KDs of the compounds have been reported, leading to a breakthrough energy barrier U_{eff}/k_B = 1025 K and a high hysteresis temperature compared with the known SMM materials.[16,34−36] Intermolecular interaction is also observed by micro-SQUID measurements, which suggests it is non-negligible even if the nearest neighboring Dy···Dy distance is as large as 8.5 Å. The largest energy barrier ever as well as the high hysteresis temperature is enabled owing to the highly axial crystal field realized in these compounds caused by the presence of two almost linearly coordinated oxygen atoms. At the same time, the crystal field due to the five equatorial ligands is relatively weak and symmetric, providing relatively weak nonaxial components of the crystal field, resulting in a high axiality in the low-lying KDs. Thus, the compounds investigated here approach the ideal situation of a pure axial compound (with zero transverse components of the crystal field), for which the blocking barriers consist solely of doublets arising from the ground atomic J-multiplet of Ln ion; because of this, they are expected to be very high and opaque. The importance of this work is that it shows the practical way to design highly efficient SMMs: One should increase the axial field from the two axial atoms and diminish the transverse field from the equatorial atoms, trying to keep the symmetry of the latter as high as possible.

EXPERIMENTAL SECTION

General Procedure. All reactions and manipulations described below were performed under aerobic conditions. The ligand *N*,*N*′-bis(2-hydroxybenzyl)-*N*,*N*′-bis(2-methylpyridy1)ethylenediamine (H_2bbpen) was prepared in excellent yield according to the reported methods.[37,38] Metal salts and other reagents were commercially available and used as received without further purification. The C, H, and N microanalyses were carried out with an Elementar Vario-EL CHNS elemental analyzer. The FT-IR spectra were recorded from KBr pellets in the range 4000−400 cm^{-1} on an EQUINOX 55 spectrometer. Thermogravimetric analysis was carried out on a NETZSCH TG209F3 thermogravimetric analyzer. X-ray powder diffraction intensities for polycrystalline samples were measured at 293 K on Bruker D8 Advance Diffratometer (Cu-K_α, λ = 1.54178 Å). An accurate yttrium/dysprosium ratio was measured using the inductively coupled plasma (ICP) atomic emission spectra analyzed by a TJA IRIS(HR) spectrometry.

[Dy(bbpen)Cl] (1). To a solution of $DyCl_3{\cdot}6H_2O$ (37 mg, 0.1 mmol) and H_2bbpen (46 mg, 0.1 mmol) in ethanol (5 mL) was dropwise added triethylamine (20 mg, 0.2 mmol). After stirring for 5 min, the resulting mixture was immediately filtrated, and the filtrate was left to stand at room temperature for slow evaporation. The product (yield ca. 50 mg, 77%), was obtained as colorless block crystal after 1 day. Elem anal. calcd: C, 51.69; H, 4.33; N, 8.61. Found: C, 51.88; H, 4.32; N, 8.51.

[Dy(bbpen)Br] (2). To a solution of H_2bbpen (46 mg, 0.1 mmol) in acetonitrile (6 mL) was added triethylamine (0.2 mmol). After stirring for 5 min, the anhydrous $DyBr_3$ (40 mg, 0.1 mmol) solid was added to generate a slightly white suspension, which was sealed in a 23 mL Teflon-lined stainless container and kept at 70 °C for 1 day and then cooled to ambient temperature at a rate of 10 °C/h to form colorless block crystals (yield ca. 45 mg, 65%). Elem anal. calcd: C, 48.39; H, 4.06; N, 8.06. Found: C, 48.43; H, 4.01; N, 8.07.

[Y(bbpen)Cl] (3). Compound **3** was prepared by analogous method from 1, replacing $DyCl_3{\cdot}6H_2O$ with $YCl_3{\cdot}6H_2O$ as starting metal(III) chloride (yield ca. 43 mg, 74%). Elem anal. calcd: C, 58.29; H, 4.89; N, 9.71. Found: C, 58.00; H, 4.95; N, 9.53.

[Y(bbpen)Br] (4). Compound **4** was prepared by analogous method from 2, replacing anhydrous $DyBr_3$ with anhydrous YBr_3 as starting metal(III) bromide (yield ca. 40 mg, 64%). Elem anal. calcd: C, 54.12; H, 4.54; N, 9.02. Found: C, 53.97; H, 4.48; N, 9.04.

Dysprosium-Doped Yttrium Materials Dy@3. The magnetically dilute sample, Dy@**3**, was obtained by combining accurately measured amounts of $DyCl_3{\cdot}6H_2O$ and $YCl_3{\cdot}6H_2O$ in a 1:19 molar ratio, following the procedure described as compound **1**.The final crystalline product with dysprosium content (~6.2%) was determined by the ICP atomic emission spectra analyzed by a TJA IRIS(HR) spectrometry.

(Dy@4). The magnetically dilute sample, Dy@**4**, was obtained by combining accurately measured amounts of anhydrous $DyBr_3$ and YBr_3 in a 1:19 molar ratio, following the procedure described as compound **2**.The final crystalline product with dysprosium content (~5.2%) was determined by the ICP atomic emission spectra analyzed by a TJA IRIS(HR) spectrometry.

X-ray Crystallography. Diffraction intensities were collected on a Rigaku R-AXIS SPIDER IP diffractometer with Mo-K_α radiation (λ = 0.71073 Å) for **1** and **2** at 150(2) K and an Oxford CCD diffractometer using mirror-monochromated Cu-K_α radiation (λ = 1.54178 Å) for **3** and **4** at 150(2) K. The structures were solved by direct methods, and all non-hydrogen atoms were refined anisotropically by least-squares on F^2 using the SHELXTL program suite. Anisotropic thermal parameters were assigned to all non-hydrogen atoms. Hydrogen atoms on organic ligands were generated by the riding mode.[39] Data have been deposited at the Cambridge Structural Database with the following CCDC numbers: [Dy(bbpen)Cl] (**1**),

DOI: 10.1021/jacs.6b02638
J. Am. Chem. Soc. 2016, 138, 5441−5450

CCDC-1416544; [Dy(bbpen)Br] (**2**), CCDC-1416543; [Y(bbpen)Cl] (**3**), CCDC-1421311; [Y(bbpen)Br] (**4**), CCDC-1421310.

Magnetic Measurements. Magnetic susceptibility measurements were collected using a Quantum Design MPMS-XL7 SQUID magnetometer and a Quantum Design PPMS-XL9 VSM. Polycrystalline samples were embedded in vaseline to prevent torqueing. AC magnetic susceptibility data measurements were performed with a 5 Oe switching field at frequencies between 1 and 1488 Hz. All data were corrected for the diamagnetic contribution calculated using the Pascal constants. The single-crystal measurements down to ultralow temperature were performed on a micro-SQUID.[40]

Ab Initio Calculation. All calculations were carried out with MOLCAS 8.0 and are of CASSCF/RASSI/SINGLE_ANISO type. The Cholesky decomposition threshold was set to 1×10^{-9} to save disk space. Active space of the CASSCF method included 9 electrons in 7 orbitals (4f orbitals of Dy^{3+} ion). All spin free states were calculated at the CASSCF level: 21 sextets, 224 quartets, and 490 doublets, while 21 sextets, 128 quartet and 130 doublet states were mixed by spin−orbit coupling within SO-RASSI, due to disk space limitations. On the basis of the resulting spin−orbital multiplets SINGLE_ANISO program computed local magnetic properties (*g*-tensors, magnetic axes, local magnetic susceptibility, etc.)

■ ASSOCIATED CONTENT

Supporting Information

The Supporting Information is available free of charge on the ACS Publications website at DOI: 10.1021/jacs.6b02638.

Additional crystal structure data, magnetic characterization, and ab initio calculations (PDF)
Crystallographic data (CIF)
Crystallographic data (CIF)
Crystallographic data (CIF)
Crystallographic data (CIF)

■ AUTHOR INFORMATION

Corresponding Authors

*ljliang1987@gmail.com
*Liviu.chibotaru@chem.kuleuven.be
*wolfgang.wernsdorfer@neel.cnrs.fr
*tongml@mail.sysu.edu.cn

Author Contributions

#These authors contributed equally.

Notes

The authors declare no competing financial interest.

■ ACKNOWLEDGMENTS

This article is dedicated to Professor Thomas C. W. Mak on the occasion of his 80th birthday. This work was supported by the "973 Project" (2014CB845602 and 2012CB821704), the NSFC (grant nos 91122032, 21371183 and 91422302), the NSF of Guangdong (S2013020013002), the Program for Changjiang Scholars and Innovative Research Team in the Universities of China. L.U. is a postdoc of the Fonds Wetenschappelijk Onderzoek-Vlaanderen and also gratefully acknowledges the INPAC and Methusalem grants of KU Leuven. Y.L. and W.W. acknowledge the EU for financial support within the FP7 FET-Proactive project MoQuaS no. 610449 and the Agence Nationale de la Recherche for project MolQuSpin, no. ANR-13-BS10.

■ REFERENCES

(1) Sessoli, R.; Gatteschi, D.; Caneschi, A.; Novak, M. A. *Nature* **1993**, *365*, 141.
(2) Christou, G.; Gatteschi, D.; Hendrickson, D. N. *MRS Bull.* **2000**, *25*, 66.
(3) Leuenberger, M. N.; Loss, D. *Nature* **2001**, *410*, 789.
(4) Bogani, L.; Wernsdorfer, W. *Nat. Mater.* **2008**, *7*, 179.
(5) Woodruff, D. N.; Winpenny, R. E. P.; Layfield, R. A. *Chem. Rev.* **2013**, *113*, 5110.
(6) Sessoli, R.; Powell, A. K. *Coord. Chem. Rev.* **2009**, *253*, 2328.
(7) Ishikawa, N.; Sugita, M.; Ishikawa, T.; Koshihara, S.-y.; Kaizu, Y. *J. Am. Chem. Soc.* **2003**, *125*, 8694.
(8) AlDamen, M. A.; Clemente-Juan, J. M.; Coronado, E.; Martí-Gastaldo, C.; Gaita-Ariño, A. *J. Am. Chem. Soc.* **2008**, *130*, 8874.
(9) Jiang, S.-D.; Wang, B.-W.; Sun, H.-L.; Wang, Z.-M.; Gao, S. *J. Am. Chem. Soc.* **2011**, *133*, 4730.
(10) Rinehart, J. D.; Fang, M.; Evans, W. J.; Long, J. R. *Nat. Chem.* **2011**, *3*, 538.
(11) Rinehart, J. D.; Fang, M.; Evans, W. J.; Long, J. R. *J. Am. Chem. Soc.* **2011**, *133*, 14236.
(12) Blagg, R. J.; Ungur, L.; Tuna, F.; Speak, J.; Comar, P.; Collison, D.; Wernsdorfer, W.; McInnes, E. J. L.; Chibotaru, L. F.; Winpenny, R. E. P. *Nat. Chem.* **2013**, *5*, 673.
(13) Liu, J.-L.; Chen, Y.-C.; Zheng, Y.-Z.; Lin, W.-Q.; Ungur, L.; Wernsdorfer, W.; Chibotaru, L. F.; Tong, M.-L. *Chem. Sci.* **2013**, *4*, 3310.
(14) Ganivet, C. R.; Ballesteros, B.; de la Torre, G.; Clemente-Juan, J. M.; Coronado, E.; Torres, T. *Chem. - Eur. J.* **2013**, *19*, 1457.
(15) Guo, Y.-N.; Ungur, L.; Granroth, G. E.; Powell, A. K.; Wu, C.; Nagler, S. E.; Tang, J.; Chibotaru, L. F.; Cui, D. *Sci. Rep.* **2014**, *4*, 5471.
(16) Gregson, M.; Chilton, N. F.; Ariciu, A.-M.; Tuna, F.; Crowe, I.; Lewis, W.; Blake, A. J.; Collison, D.; McInnes, E. J. L.; Winpenny, R. E. P.; Liddle, S. *Chem. Sci.* **2016**, *7*, 155.
(17) Ungur, L.; Chibotaru, L. F. *Phys. Chem. Chem. Phys.* **2011**, *13*, 20086.
(18) (a) Cole, K. S.; Cole, R. H. *J. Chem. Phys.* **1941**, *9*, 341. (b) Rinehart, J. D.; Long, J. R. *Chem. Sci.* **2011**, *2*, 2078.
(19) Le Roy, J. J.; Ungur, L.; Korobkov, I.; Chibotaru, L. F.; Murugesu, M. *J. Am. Chem. Soc.* **2014**, *136*, 8003.
(20) Ungur, L.; Le Roy, J. J.; Korobkov, I.; Murugesu, M.; Chibotaru, L. F. *Angew. Chem., Int. Ed.* **2014**, *53*, 4413.
(21) Wernsdorfer, W. *Supercond. Sci. Technol.* **2009**, *22*, 064013.
(22) Nguyen, T. N.; Wernsdorfer, W.; Shiddiq, M.; Abboud, K. A.; Hill, S.; Christou, G. *Chem. Sci.* **2016**, *7*, 1156.
(23) Yang, E.-C.; Wernsdorfer, W.; Zakharov, L. N.; Karaki, Y.; Yamaguchi, A.; Isidro, R. M.; Lu, G.-D.; Wilson, S. A.; Rheingold, A. L.; Ishimoto, H.; Hendrickson, D. N. *Inorg. Chem.* **2006**, *45*, 529.
(24) Wernsdorfer, W.; Aliaga-Alcalde, N.; Hendrickson, D. N.; Christou, G. *Nature* **2002**, *416*, 406.
(25) Jiang, S. D.; Wang, B. W.; Su, G.; Wang, Z. M.; Gao, S. *Angew. Chem., Int. Ed.* **2010**, *49*, 7448.
(26) Orbach, R. *Proc. R. Soc. London, Ser. A* **1961**, *264*, 458.
(27) Liddle, S. T.; van Slageren, J. *Chem. Soc. Rev.* **2015**, *44*, 6655.
(28) Shrivastava, K. N. *Phys. Status Solidi B* **1983**, *117*, 437.
(29) Aquilante, F.; De Vico, L.; Ferré, N.; Ghigo, G.; Malmqvist, P.-å.; Neogrády, P.; Pedersen, T. B.; Pitoňák, M.; Reiher, M.; Roos, B. O.; Serrano-Andrés, L.; Urban, M.; Veryazov, V.; Lindh, R. *J. Comput. Chem.* **2010**, *31*, 224.
(30) Chibotaru, L. F.; Ungur, L. *J. Chem. Phys.* **2012**, *137*, 064112.
(31) *MOLCAS manual*; MOLCAS; Lund University: Lund, Sweden, http://www.molcas.org/documentation/manual/.
(32) Ungur, L.; Thewissen, M.; Costes, J.-P.; Wernsdorfer, W.; Chibotaru, L. F. *Inorg. Chem.* **2013**, *52*, 6328.
(33) Garanin, D. A.; Chudnovsky, E. M. *Phys. Rev. B: Condens. Matter Mater. Phys.* **1997**, *56*, 11102.
(34) Liu, J.-L.; Wu, J.-Y.; Chen, Y.-C.; Mereacre, V.; Powell, A. K.; Ungur, L.; Chibotaru, L. F.; Chen, X.-M.; Tong, M.-L. *Angew. Chem., Int. Ed.* **2014**, *53*, 12966.
(35) Liu, J.-L.; Wu, J.-Y.; Huang, G.-Z.; Chen, Y.-C.; Jia, J.-H.; Ungur, L.; Chibotaru, L. F.; Chen, X.-M.; Tong, M.-L. *Sci. Rep.* **2015**, *5*, 16621.

DOI: 10.1021/jacs.6b02638
J. Am. Chem. Soc. 2016, 138, 5441−5450

(36) Chen, Y.-C.; Liu, J.-L.; Ungur, L.; Liu, J.; Li, Q.-W.; Wang, L.-F.; Ni, Z.-P.; Chibotaru, L. F.; Chen, X.-M.; Tong, M.-L. *J. Am. Chem. Soc.* **2016**, *138*, 2829.
(37) Neves, A.; Erthal, S. M. D.; Vencato, I.; Ceccato, A. S.; Mascarenhas, Y. P.; Nascimento, O. R.; Horner, M.; Batista, A. A. *Inorg. Chem.* **1992**, *31*, 4749.
(38) Wong, E.; Liu, S.; Rettig, S.; Orvig, C. *Inorg. Chem.* **1995**, *34*, 3057.
(39) Sheldrick, G. M. *Acta Crystallogr., Sect. A: Found. Crystallogr.* **2008**, *64*, 112.
(40) Wernsdorfer, W. *Supercond. Sci. Technol.* **2009**, *22*, 064013.

DOI: 10.1021/jacs.6b02638
J. Am. Chem. Soc. 2016, 138, 5441−5450